Article

Cascading Landslide: Kinematic and Finite Element Method Analysis through Remote Sensing Techniques

Claudia Zito [1], Massimo Mangifesta [2], Mirko Francioni [3], Luigi Guerriero [4], Diego Di Martire [4], Domenico Calcaterra [4] and Nicola Sciarra [2,*]

[1] Department of Engineering and Geology, Gabriele D'Annunzio University of Chieti-Pescara, 66100 Chieti, CH, Italy; claudia.zito@unich.it

[2] Department of Psychological, Health, and Territorial Sciences, Gabriele D'Annunzio University of Chieti-Pescara, 66100 Chieti, CH, Italy; mmangifesta@unich.it

[3] Department of Pure and Applied Sciences, Carlo Bo University of Urbino, 61029 Urbino, PU, Italy; mirko.francioni@uniurb.it

[4] Department of Earth, Environmental and Resource Sciences, Federico II University of Naples, 80138 Napoli, NA, Italy; luigi.guerriero2@unina.it (L.G.); diego.dimartire@unina.it (D.D.M.); domcalca@unina.it (D.C.)

* Correspondence: nicola.sciarra@unich.it

Abstract: Cascading landslides are specific multi-hazard events in which a primary movement triggers successive landslide processes. Areas with dynamic and quickly changing environments are more prone to this type of phenomena. Both the kind and the evolution velocity of a landslide depends on the materials involved. Indeed, rockfalls are generated when rocks fall from a very steep slope, while debris flow and/or mudslides are generated by fine materials like silt and clay after strong water imbibition. These events can amplify the damage caused by the initial trigger and propagate instability along a slope, often resulting in significant environmental and societal impacts. The Morino-Rendinara cascading landslide, situated in the Ernici Mountains along the border of the Abruzzo and Lazio regions (Italy), serves as a notable example of the complexities and devastating consequences associated with such events. In March 2021, a substantial debris flow event obstructed the Liri River, marking the latest step in a series of landslide events. Conventional techniques such as geomorphological observations and geological surveys may not provide exhaustive information to explain the landslide phenomena in progress. For this reason, UAV image acquisition, InSAR interferometry, and pixel offset analysis can be used to improve the knowledge of the mechanism and kinematics of landslide events. In this work, the interferometric data ranged from 3 January 2020 to 24 March 2023, while the pixel offset data covered the period from 2016 to 2022. The choice of such an extensive data window provided comprehensive insight into the investigated events, including the possibility of identifying other unrecorded events and aiding in the development of more effective mitigation strategies. Furthermore, to supplement the analysis, a specific finite element method for slope stability analysis was used to reconstruct the deep geometry of the system, emphasizing the effect of groundwater-level flow on slope stability. All of the findings indicate that major landslide activities were concentrated during the heavy rainfall season, with movements ranging from several centimeters per year. These results were consistent with numerical analyses, which showed that the potential slip surface became significantly more unstable when the water table was elevated.

Keywords: cascading landslides; slope stability; InSAR interferometry; pixel offset; finite element analysis; numerical modeling

1. Introduction

Cascading landslides can be described as series of landslides that occur sequentially in a chain reaction, typically initiated by a triggering event such as heavy rainfall, seismic activity, or anthropogenic activities such as excavation or blasting. This phenomenon

starts when an initial landslide destabilizes the surrounding terrain, leading to subsequent landslides that may intensify the damage caused by the initial event or create a predisposed environment for subsequent slope failures [1]. These subsequent landslides can be triggered by slope overloading caused by debris generated by the initial event or changes in the terrain conditions resulting from an initial landslide [2]. As a result, cascading landslides can amplify the damage caused by the initial event and propagate the instability along a slope; common consequences of cascading landslides are landslide dams with consequent flooding [3]. Notable examples of this kind of process were observed during the Nepal 2015 earthquake. On 25 April 2015, in Lamjung (Nepal), a magnitude 7.8 earthquake triggered a series of landslides across large mountainous areas of the country, blocking rivers, causing floods, and resulting in considerable damage and human loss [4]. The geological conditions of the material involved in the triggering event are fundamental to determining the velocity and the evolution of cascading landslides. For example, heavy rainfall can saturate the soil, increasing its weight and reducing its stability, while seismic activity can lead to ground shaking, further destabilizing the slope. Even wildfires can trigger cascading landslides. Indeed, fire action reduces the vegetation and the infiltration capacity of soil. These aspects alter the saturation trends and timing, thereby influencing slope stability [5]. The mechanisms can include sliding, which occurs when a layer of soil moves along a sliding plane, often favoring clayey or highly saturated soils, and rolling, which involves the movement of larger debris, such as rocks or boulders, along the surface of the terrain. Bouncing is another mode that can occur, particularly with smaller or irregularly sized debris, where the debris bounces or hops along the surface of the terrain, propelled by the force of the flow [6]. During a cascading landslide, the debris and sediment generated by the initial landslide can be transported in different modes or flow regimes, depending on the characteristics of the terrain and the involved materials. Gravity-driven flow is a common mode of debris transport, where sediments move downslope under the influence of gravity. The velocity of the flow can vary, depending on factors such as the amount of water present in the debris and the slope of the terrain [7]. The transport of debris and sediment can significantly alter the shape and characteristics of the surrounding terrain. Debris accumulation can obstruct watercourses, roads, or inhabited areas, posing a threat to infrastructure and human populations. The movement of debris can also lead to erosion of the surrounding terrain, causing soil loss and changes in local topography. Additionally, cascading landslides can interact with existing infrastructure along their path, increasing the risk of damage and human loss. Buildings, bridges, roads, and other infrastructure can be impacted by subsequent landslides [8], resulting in structural damage or even destruction. Debris deposits can also block roads, railways, or watercourses, disrupting communication routes and hampering rescue and evacuation efforts [9]. The fast movement of debris and sediment poses a risk to human safety, as people along the path of a cascading landslide can be injured or killed [10]. The velocity of cascading landslides exhibits significant variability depending on the mechanisms involved in the slope failure process. Factors such as the slope gradient, materials involved (kind and volume), and triggering factors play crucial roles in determining the velocity of movement [11]. Landslides initiated by shallow translational sliding or surface erosion tend to move at slower velocities, typically ranging from centimeters to meters per year. By contrast, events triggered by rapid failure mechanisms such as rockfall, debris flow, or liquefaction can attain velocities exceeding 10 m/s. Moreover, the presence of water, either from precipitation or groundwater, can further influence landslide velocity by increasing the weight of the sliding mass and reducing frictional resistance [8]. Notable examples highlighting the destructive potential of cascading landslides include Kedarnath (Indian Himalayas), where in 2013, heavy rainfall caused a series of landslides and floods, destroying entire villages and thousands of deaths [12]. In 2017, Sierra Leone experienced a series of landslides triggered by heavy rainfall, causing a high number of casualties and widespread destruction of homes and infrastructure [13]. A further example is the Morino-Rendinara landslide [14]. This landslide developed along the Ernici Mountains,

near the border between the Abruzzo and Lazio regions, in the Apennines Mountain range, a typical environment where cascading landslides can be observed in Italy.

Remote sensing techniques are a fundamental method for the study and monitoring of cascading landslides, such as the Morino-Rendinara landslide. These techniques offer significant advantages in understanding the complex dynamics and kinematics of such events, particularly when integrated with traditional methods like borehole and numeric analysis. Remote sensing allows for the continuous observation of large and often inaccessible areas, providing valuable data on deformation, displacement, and changes over time. These data are essential for reconstructing subsurface models and identifying potential risk areas. Additionally, remote sensing technologies enable observation of the smallest ground movements that might precede larger landslide events, offering early warning capabilities that are critical for protecting infrastructure and human lives. With the use of remote sensing in landslide studies, researchers can achieve a more comprehensive understanding of the processes and more effective management of landslides.

The Morino-Rendinara cascading landslide (Figure 1) is one of the most significant examples of cascading landslides in terms of landslide mechanism differentiation, impact, and the involved surface. The study aims to comprehensively understand the kinematics of this cascading landslide by focusing on the mechanisms characterizing its components. To reconstruct the model, traditional techniques, field activities, remote sensing, and numerical modeling [15] were integrated. These methodologies were used to study the complex kinematics involved in the Morino-Rendinara landslide with high precision and accuracy, ultimately contributing to better risk assessment and mitigation strategies for similar landslide-prone areas.

Figure 1. Aerial and field images of the Morino-Rendinara landslide that are representative of the impact of the landslide on the environment. (**a**) Overview of phenomenon taken from Google Earth [16] satellite images of 13 June 2022, from the upper sector near Morino Hamlet to the lower sector, Liri River, and deep-seated rotational slide; (**b**) Details of rockfall/avalanches sector; (**c**) Debris flow source area; (**d**) Debris flow transit zone; (**e**) Lowest debris flow transit zone; (**f**) Liri River dam; and (**g**) Effect on Liri River dam.

2. Study Area

The area is located in the upper sector of the Roveto Valley, near the borders of the Abruzzo and Lazio Apennine Mountains, on the eastern side of the Liri River Valley, in central Italy. It extends between the municipalities of Morino and San Vincenzo Valle Roveto, both of which were affected by the debris flow event of March 2021 (Figure 2).
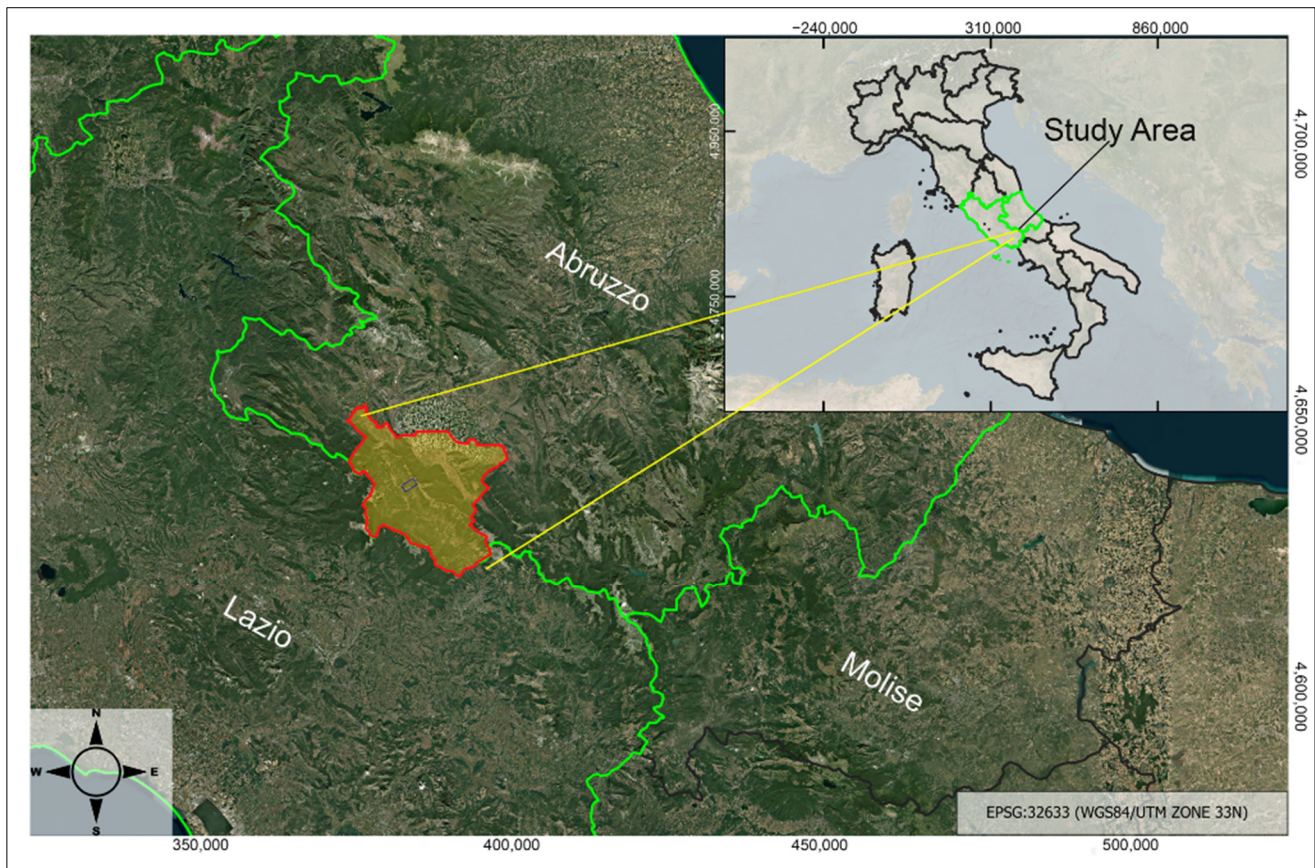

Figure 2. Geographical location of Morino-Rendinara. Green lines indicate the regional boundaries; red lines indicate the municipality of Morino, Castronovo, and San Vincenzo Valle Roveto composing the involved municipality; the light blue square indicates the landslide and the study area.

The Liri River Valley is composed primarily of Messinian siliciclastic deposits (Figure 3), which were deformed by the active tectonics of the Apennines and the deformation caused by glaciation. Additionally, there are secondary components of polygenic breccias and puddingstones [17,18]. The Ernici Mountains and the Simbruini Mountains, together, form an over thrusting ridge of Jurassic-Miocene carbonate units over the Messinian siliciclastic deposits in the Liri River Valley [19]. The Jurassic-Miocene carbonate units, particularly the Miocene sections, within the study area exhibit significant jointing due to active normal faults. These units override the siliciclastic deposits (composed of clay and sandstone), forming the base structure of the Liri River, with a tectonic contact characterized by a low angle (10°–20° with a W-SW dip component) [20]. This low-angle contact has been interpreted by various authors over the last decades as the result of differential north-eastward translation and anticlockwise rotation of the carbonate structure [18]. This rotation is characterized by greater shortening in the southern sector [21]. Along the main Mesozoic slope, the gradient transitions from 60° to an average of 18°. In areas with the least steep inclines, the presence of fractured slope materials has led to sediment accumulation, forming slope deposits [16–21]. Additionally, the region features Holocene fluvial deposits, illustrated in Figure 4, which include fluvial terraces and detrital cone formations. These deposits arise from the removal of debris by water along the slopes and the Liri River within

the lower sectors of the valley [22]. Due to their distinct origins, these deposits exhibit heterogeneity, resulting in layers with varying permeability, which is further influenced by differences in grain size [17]. As a result of these deposits and an extremely fractured and permeable carbonate aquifer, when large volumes of water migrate from this aquifer to the Messinian deposits, suspended aquifers tend to form. These aquifers occasionally emerge as springs along the slope due to variations in the grain sizes of the deposits and contrasts in permeability.
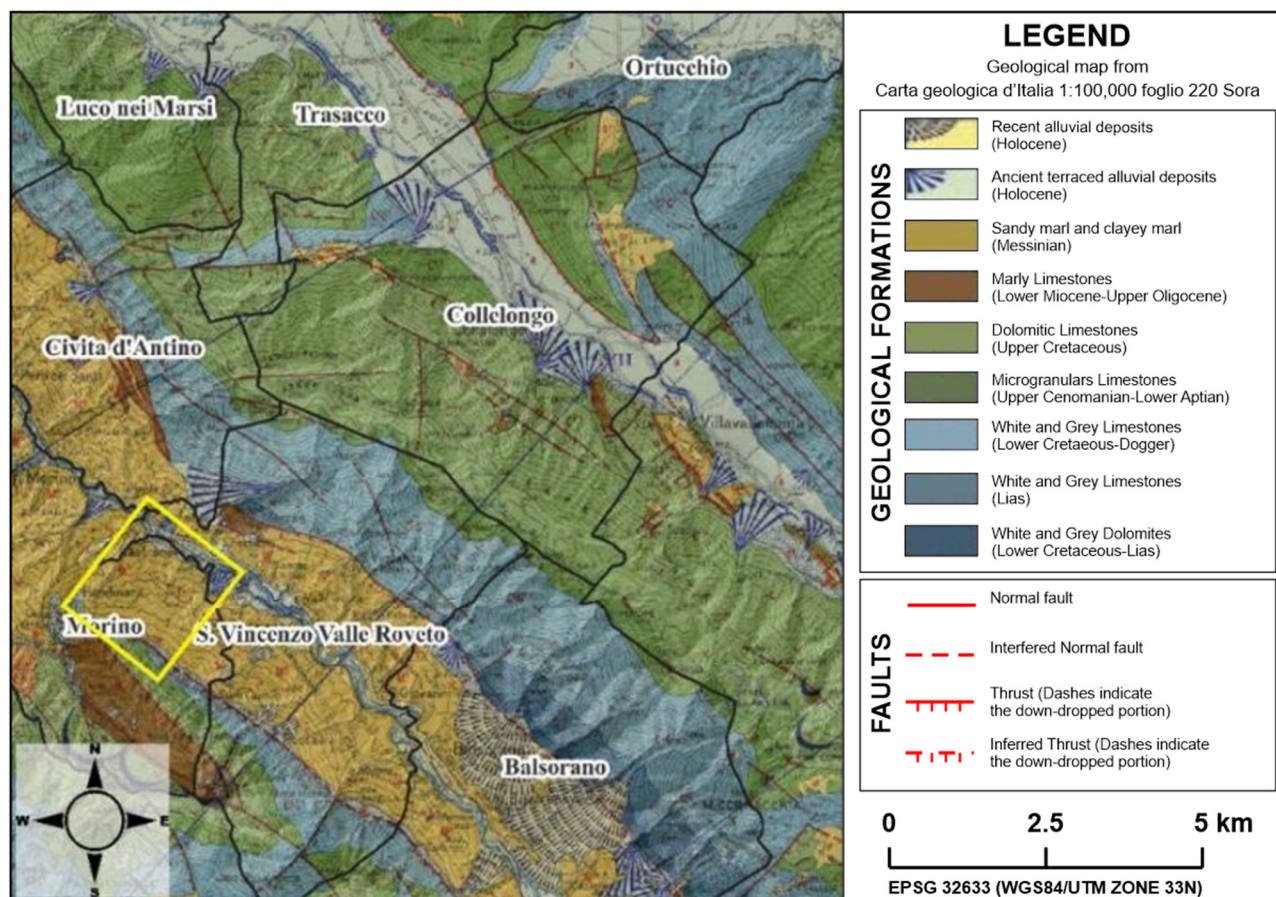

Figure 3. Geological map extract from the CARG (Geological CARtography Map n.220 Sora) Project [22], with indications of the geological formations and tectonic processes present in the area.

In the area, a significant amount of water emerges from the tectonically highly fractured aquifer. In some cases, when the detritus and marly formations obstruct natural watercourses, springs may form or water may accumulate within this layer, exacerbating local instability [14,23]. This was observed in the source area of the last debris flow reactivation in March 2021, where a high-flow spring emerged from the source zone of the debris flow characterized by the cover material (Figure 1c).

As part of the Civil Protection Landslide Risk Assessment Program, some geognostic and geophysics surveys were realized in the area. In the upper sector, the stratigraphic map shows the coverage layer composed by heterogeneous and low-cohesive deposits. While in the middle sector of the slope, the materials are more compact, as shown in the geological map. In this work, four boreholes were considered to gain a comprehensive understanding of the geotechnical composition and sub-surface characteristics of the materials comprising the landslide and the surrounding area. The drilling data were interpolated to reconstruct two representative sections of the landslide area (Figure 4).
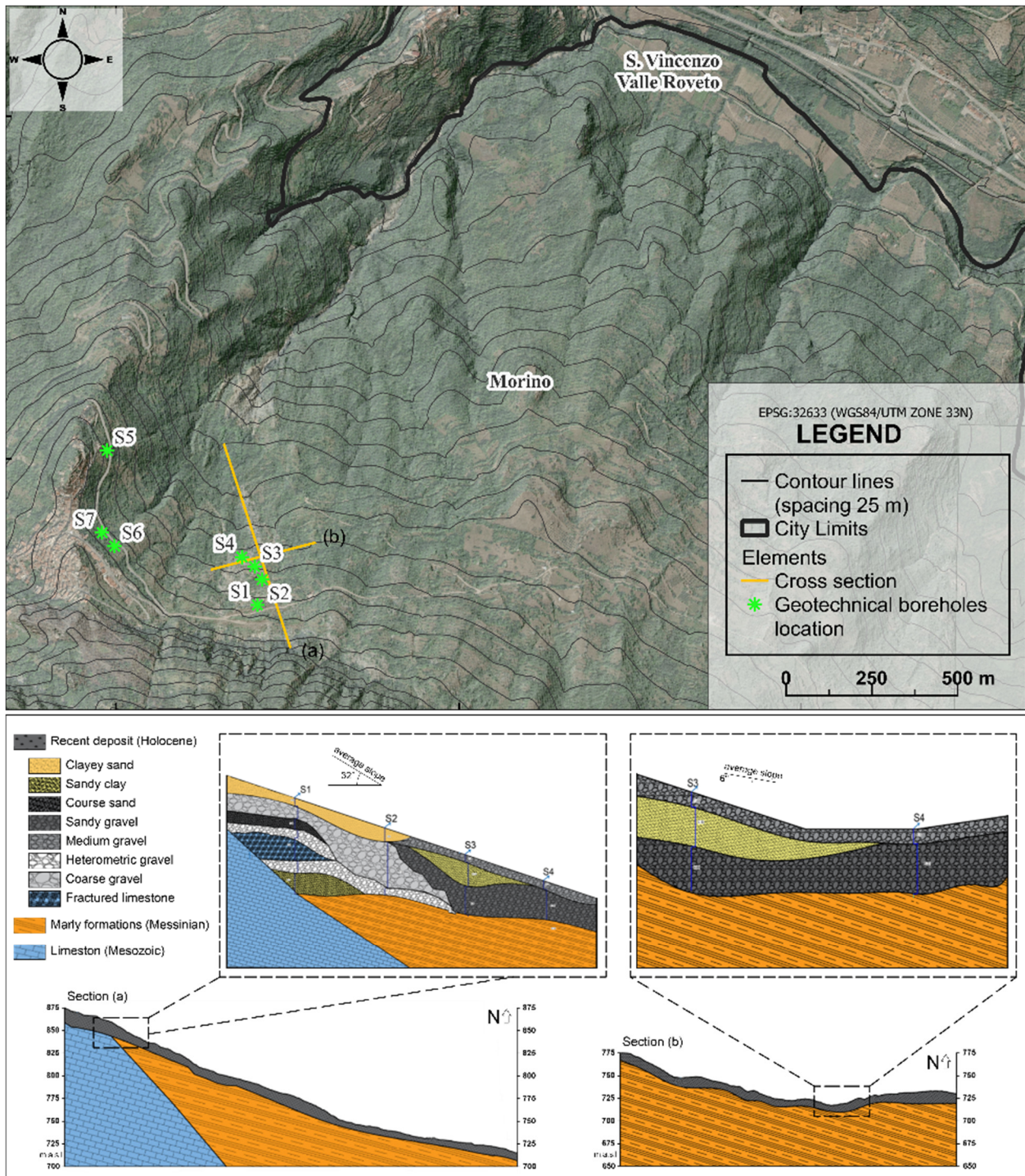
Figure 4. Maps of the survey and debritic cover layer reconstruction using cross-sections to empathize the heterogeneity of deposits covering the substrate. (a) The section develops on maximum slope line. (b) The section develops on perpendicular direction.

According to the geological scientific literature, in the area [14,19], the local features exhibit an unstable accumulation of detritus covering two primary formations: Mesozoic limestone and Messinian marly formations. The thickness of the cover layer typically ranges between 12 and 22 m, with materials varying in size and distribution. It is noted that all recorded materials contain limestone, suggesting that this cover material originates from fractured limestone formations, which constitute the steeper areas of the region affected by numerous rockfalls and avalanches [19,20].

3. Materials and Methods

This study aims to provide insight into the geological and hydrogeological conditions contributing to slope instability (through specific FEM analyses), characterized by the tec-tonic contact overriding an arenaceous clayey (Messinian) less permeable aquifer. This aquifer is covered by an unstable and heterogeneous slope deposit originating from the rockfall deposits from Mesozoic carbonaceous rocks.

In the upper part of the slope, a detailed UAV investigation was carried out. We used a DJI drone equipped with an L1D-20c camera (10.26 mm focal length) to acquire 448 images. The camera resolution was 5472×3648 pixels, with a pixel size of 2.41×2.41 μm. The images had an overlapping equal to 80%. The mean flying altitude was 92.9 m above the local station, and six ground control points were used to align the model. All images were processed with Metashape pro v1.2.

These insights were further enhanced by implementing advanced techniques, such as interferometry using SENTI-NEL-1 from European Space Agency (ESA) images covering the period from 2020 to 2023, processed by Subsidence software v28.03 [24–26]. In addition, to supplement the kinematics analysis, pixel offset analysis based on a simple correlation procedure applied to Google Earth high-resolution images was carried out to estimate the cumulative displacement from 2016 to 2022 [27], covering the last debris flow reactivation. Finally, a slope stability analysis was carried out to better understand the role of underground water circulation and estimate the factor of safety (FoS) along the slope through the combination of FEM (finite element methods) and SRM (strength reduction methods). The application of SRM offers several practical advantages [28,29]. Firstly, it provides a systematic approach to evaluate slope stability by simulating failure mechanisms in a controlled manner. Secondly, it allows engineers to assess the sensitivity of slope stability to changes in shear strength parameters, thus aiding in risk assessment and mitigation strategies. Moreover, SRM facilitates the identification of critical failure surfaces and potential failure zones within the slope, enhancing the overall understanding of slope behavior under varying conditions [30]. Due to the complexity of the analyzed case study, a conceptual map of the main study phases was produced and is illustrated in Figure 5.
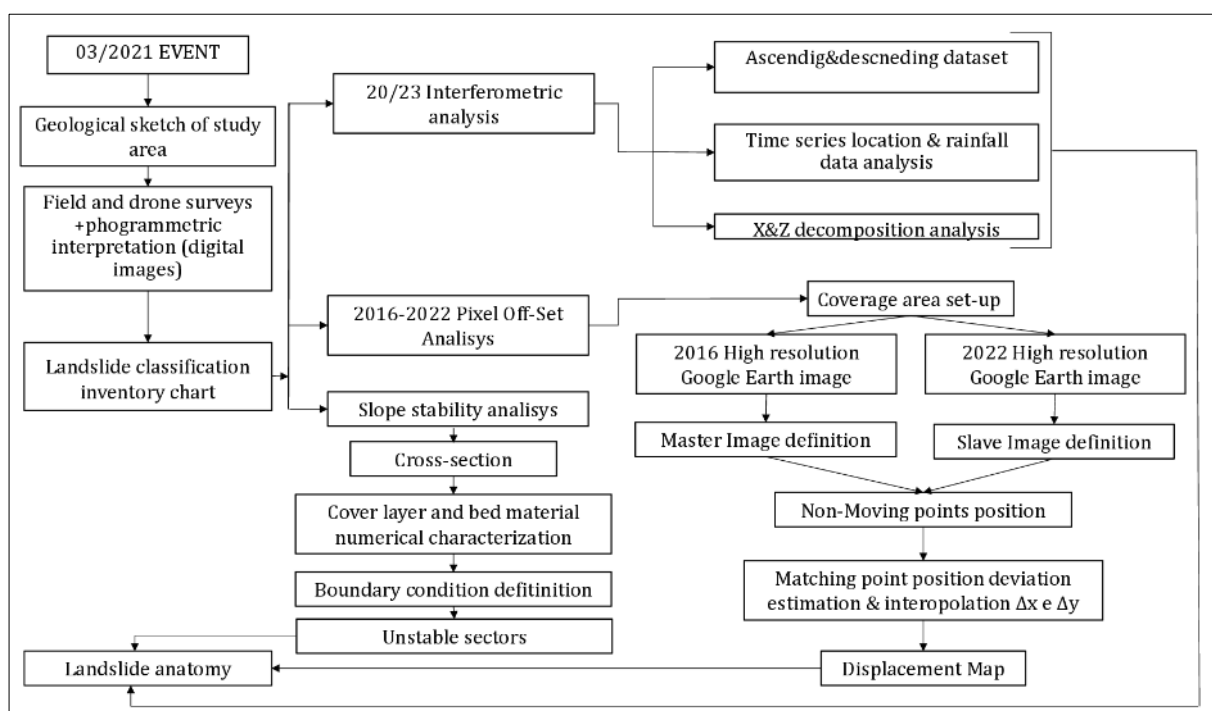

Figure 5. Conceptual flow chart of the work phases.

3.1. Field and Geomorphological Interpretation

To gain a deeper understanding of the landslide characteristics, drones equipped with high-resolution cameras were employed. Through the utilization of this cutting-edge technology, high-definition aerial images were captured, enabling a detailed analysis of the terrain morphology and landslide features [31]. Specifically, the collected images were processed, allowing for the precise identification and mapping of unstable areas, active sliding zones, and deformative structures within the study area. To integrate the analysis obtained from traditional field activities and drone surveys, a photogrammetric interpretation of the collected images was conducted. This approach involved the use of specialized software to analyze and process the aerial images, aiming to accurately identify and map the geomorphological features and deformative structures of the landslide. The analysis of drone-acquired images was augmented by cross-referencing survey data and satellite imagery from Google Earth. This comprehensive approach encompassed both contemporary and archival satellite imagery, enabling a longitudinal examination of landslide mechanisms. By integrating drone imagery with ground surveys and satellite data, we were able to obtain a detailed understanding of the temporal evolution of landslide events.

3.2. SAR Interferometry

Using differential interferometry techniques (DInSAR) [26], the deep-seated component of the Morino-Rendinara landslide was analyzed. The SENTINEL-1 dataset images were obtained from the European Space Agency (ESA), as part of the Copernicus program in collaboration with European Commission (EC). SENTINEL satellites have provided information and support for earth observation and environmental monitoring, particularly for emergency management purposes [24]. In this case, the analyzed dataset comprises:

- A total of 96 images acquired in ascending geometry, covering the period from 3 January 2020 to 24 March 2023, with an incidence angle of 39.5°, generating 435 interpherograms. The image acquired on 6 September 2021 was automatically set as the master image.
- A total of 107 images acquired in descending geometry, covering the period from 9 January 2020 to 30 March 2023, with an angle of 43.6° to the vertical inclination, generating 484 interpherograms. The image acquired on 9 March 2021 was automatically set as the master.

These images were processed using the "coherent pixels techniques" (CPT) described in [25] and implemented by Igelsias [32], along Temporal Phase Coherence (TPC) at the Remote Sensing Laboratory (RSLab) of the Universitat Politècnica de Catalunya (UPC) [25]. This algorithm allows for the development of the entire interferometric chain using image pairs with reduced spatial and temporal baselines, thus characterized by a better phase response, and implemented in Subsidence software v28.0. These algorithms allow for the development of the interferometric process using images coupled with a spatial and chronological baseline, resulting in a high phase response. For this work, all images were used to generate interferograms of both ascending (Figure 6a) and descending images (Figure 6b).

The process involved generating the interferograms from the available image dataset, selecting reflector targets (RTs) with a fixed phase value estimated as stable electromagnetic response, and estimating the average velocity and displacement of chosen points during the observation period. CPT allows the selection of reflector targets (equivalent to permanent scatterers) around the area of interest, exploiting the temporal phase coherence (TPC) estimator, which obtains much more valid PSs than the classical dispersion amplitude (DA) method. The TPC can be used to evaluate the quality of a pixel from the behavior of the phase noise, along the stack of differential interferograms. To achieve this, the neighboring pixels are used, assuming, in theory, the spatial low-pass behavior of all deterministic terms in the vicinity of the pixel for which the TPC is being estimated. The phase of the neighboring pixels is estimated by averaging their complex values but excluding the central pixel. All phase components, apart from noise, are assumed to be spatially low-pass (R1).

The reflectors' spatial positioning involves a conversion from the SAR (Range-Azimuth) reference system to project reference system (WGS84-UTM33N), which may be affected by a positioning error along the North–South and East–West directions of $+/-5$ m, and along the vertical direction of $+/-1.5$ m. Possible external interference, such as by atmospheric agents or decorrelation noise, can produce an error in on the order of $+/-2$ mm/year.
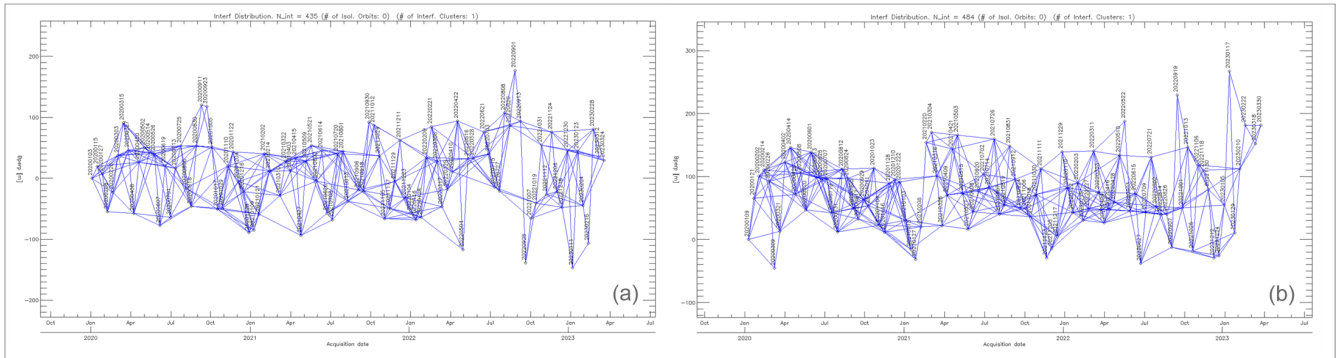

Figure 6. Spatiotemporal baseline map of SBAS-InSAR interferometric data of ascending track (**a**) and descending track (**b**).

SAR satellites acquire information following specific North–South orbits (semi-polar) [24]. Due to this acquisition strategy, positive values in ascending geometry indicate that targets are moving closer to the satellite along the East–West direction. Conversely, in descending geometry, negative values indicate that the targets are moving away from the satellite in the West–East direction. Using this information, it is possible to obtain the West–East component and the vertical component by knowing the cosine values derived from image acquisition. To obtain these components, a specific MATLAB [33] script was used in this work. The first step involved grid construction, which in this case was set as a cell size of 30 m (allowed by using MATLAB code [33]). After choosing the grid size, the script automatically calculated the RT in ascending and descending geometries, intersecting each cell and the mean value. Depending on the number of RTs (in ascending and descending geometries), a different formula was used from that in [34] (Table 1).

Table 1. Synthesis the different Cascini formulas applied [34]. "Yes" indicates the presence of corresponding geometry in the grid cell, "No" indicates the absence of corresponding geometry in the grid cell. Where $Rate_{asc}$ and $Rate_{desc}$ are the velocities obtained from ascending and descending dataset analyses, respectively; v is the velocity; and ϑ is the incident angle.

Ascending	Descending	Applied Formula
Yes	Yes	$v_z = \dfrac{(Rate_{desc} \times sx_{asc}) - (Rate_{asc} \times sx_{desc})}{(sx_{asc} \times sz_{desc}) - (sx_{desc} \times sz_{asc})}$
Yes	No	$v_{zasc} = \dfrac{Rate_{asc}}{cosin(\vartheta_{asc})}$
No	Yes	$v_{zasc} = \dfrac{Rate_{desc}}{cosin(\vartheta_{desc})}$

Due to landslide characteristics, the main component analyzed is the vertical one. Therefore, this formula does not require correction to the main reference system, as in the case of the horizontal component.

3.3. Pixel Offset

To estimate the movements during the period from 2016 to 2022, where interferometric data lacked temporal coverage and were intrinsically limited, for example, due to the orientation landslide to the line of sight (LOS), an algorithm (developed by Guerriero [27]) that estimates the displacement of pixels in Google Earth [16] high-resolution digital images was employed. Using this algorithm, the middle-lower and north-east sectors of the slope

were investigated using Google Earth imagery [35]. Initially, the area of interest (AOI) was delineated using QGIS 3.28 software [36] with a polygon measuring 2000 × 2000 m in size and a H–L ratio around 1 [37]. The images covered were saved in JPEG format with a quality of 4800 × 2674 pixels. The ground sampling distance of the images, according to the number of pixels composing the image and length of the study area was 0.5 m/pixel (R1). The satellite images were dated 13 June 2016 (before the last recorded debris flow reactivation) and 7 January 2022 (after the event). The acquisition dates depended on the clarity of the available images. Following the master/slave logic of the digital image correlation technique, the 2016 (less recent) image was set as the master image, and consequently, the 2022 image (more recent) was set as the slave image. To estimate the error, the maximum bidirectional forward–backward threshold was set at 0.05 pixels. This helped to eliminate points that could not be reliably traced. The selected images were exported in Geo-Tiff format, with two different resolutions. The first set of images, consisting of the master and slave images, was exported in a pixel size resolution of 0.5 m.

A second set, containing only the master image, was exported in a resolution with which each pixel equated to 50 m on the ground. This value represented the prospective grid used to estimate the final displacement mapping. The first high-resolution dataset was utilized directly for supervising the tracking analyses. Consequently, the second one was only employed for successfully carrying out the mapping process. The derived images were analyzed by a specific procedure developed for MATLAB® [33]. The process was based on the identification of specific characteristics (angular points), using the Kanade–Lucas–Tomasi (KLT) feature tracking algorithm [38]. These methods enabled the acquisition of displacement in vector forms, displacement components, graphics depicting the distribution of bidimensional displacement, and displacement field maps [39]. The algorithm's parameterization was completed using a trial-and-error approach to maximize the number of trackable angular points and minimize displacement error. The minimum accepted quality of angular points in the image, expressed as a fraction of the maximum angle value, was equal to 0.01.

3.4. Rainfall Analyses

To identify possible landslide activation, a graphical comparation between rainfall data and time series derived from interferometric data was conducted. Rainfall data were obtained from the Abruzzo Region Department of Government of the Territory and Environmental Policies-Civil Protection Activity Planning Service–Hydrographic and Tide Gauge Office [40]. Rainfall data were acquired with a sixty second interval. Data were collected from the San Vincenzo Valle Roveto meteorological station with code 496700, situated in the province of L'Aquila, approximately fourteen kilometres from the study area. This station was selected because other meteorological stations were located farther than 25 km from the study area. Furthermore, the absence of nearby peaks or high mountains ensures a locally uniform distribution of rainfall, making the data suitable for time series analysis. The rainfall data had a step acquisition of 60 s. The analyzed rainfall data covered the time laps starting from 1 January 2020 to 31 December 2023. The dataset comprised recorded rainfall data with a time lapse of 1 min. These data were statistically analyzed to calculate the cumulative rainfall for the analysis period, determine the maximum values, and identify the highest monthly rainfall and the five consecutively rainiest days within the analyzed period.

3.5. Slope Stability Analysis

The slope stability analysis was embarked upon to assess the specific impact of the water table on the instability of the cover layer. This analysis integrated data from borehole logs and the geological literature to estimate the thickness of the cover layer developed on fractured limestone and marly formations. ADONIS software (v. 2.5.5), an open-source finite element program, was employed for this analysis. Finite element analysis (FEA) [41] was utilized to provide an automatic factor of safety (FoS) using the strength reduction

method (SRM), a computational technique widely applied in geotechnical engineering for slope stability assessment [29]. The combination of finite element methods (FEM) with the strength reduction method (SRM) offers a significant opportunity to assess deformation distribution along a slope and predict its long-term evolution of stability. The strength reduction method (SRM) is widely recognized in finite element slope stability analysis [28]. It operates based on iteratively reducing the cohesion (c′) and the friction angle (ϕ′) of the soil until the slope undergoes failure. This failure is defined by the emergence of a shear slip surface, accompanied by the development of strain from the lower to the upper sector of the slope. The core principle of SRM is its capability to model the gradual failure of slopes through a systematic reduction in shear strength parameters until instability is reached. The essence of SRM lies in its ability to simulate the progressive failure of slopes by systematically decreasing the shear strength parameters until instability occurs. This technique acknowledges the inherent difficulty in tracing the exact failure slip surface in finite element analysis, which primarily relies on stress-based failure criteria [28]. Consequently, SRM assumes a direct correlation between the failure mechanism of the slope and the development of shear strain. It further postulates the existence of a shear strength dependency on strain, where the reduction in shear strength enhances the strain development in the slope. The slope model is discretized into finite elements, with each element representing a segment of the slope. This approach guarantees that resolution can be focused in areas where greater precision is needed, while also optimizing computational resource usage. Material properties, including cohesion, friction angle, and pore water pressure, are assigned to these elements.

In this analysis, the soil was discretized using a triangular mesh of 5 m spacing to highlight the significance of the cover layer, averaging from 12 to 22 m in thickness. The geotechnical parameters for the materials were considered to be iso-elastic for the substrate unit and Mohr–Coulomb deformation for the cover layer, as synthesized in Table 2. Due to uncertainty regarding the water table height, four distinct scenarios were examined, considering the influence of the water table as a primary stressor affecting the slope stability analysis.

Table 2. Synthetic table of parameters employed to build the finite element model for slope stability analysis in ADONIS code.

Parameter	Mesozoic Limestone	Messinian Clay	Cover Layer
Unit weight (kg/m^3)	2750	2200	2300
Young (Pa)	1.2×10^{10}	3.1×10^9	1.5×10^9
Poisson	0.30	0.25	0.25
ϕ (°)	-	-	27
c (Pa)	-	-	1.8×10^4
Type	Iso-elastic	Iso-elastic	Mohr–Coulomb
Shear Modulus (Pa)	4.6×10^9	1.2×10^9	6.0×10^8
Bulk Modulus (Pa)	1.0×10^{10}	2.1×10^9	1.0×10^9

4. Results

4.1. Field Observations, Imaging Interpretation, and Pixel Offset Results

This chart illustrates the different possible active kinematics in the study area based on geomorphological evidence [42]. To provide a comprehensive understanding of the principal mechanisms in the upper sector, interferometric and pixel offset data were analyzed. According to Figure 7, in the upper sector, there was evidence of a rockfall, while in the middle sector, there was evidence of a deep-seated rotational slide. Additionally, in the middle/lower sector, there was evidence of debris flow. Rockfalls and avalanches play important roles as sources of material and as predisposing factors for landslides. The falling of materials contributes to increasing the cover layer weight and potentially affecting the stability of the slope by adding more load to it. Additionally, variations in the water table level can influence the pore pressure in the slope and increase the instability conditions.
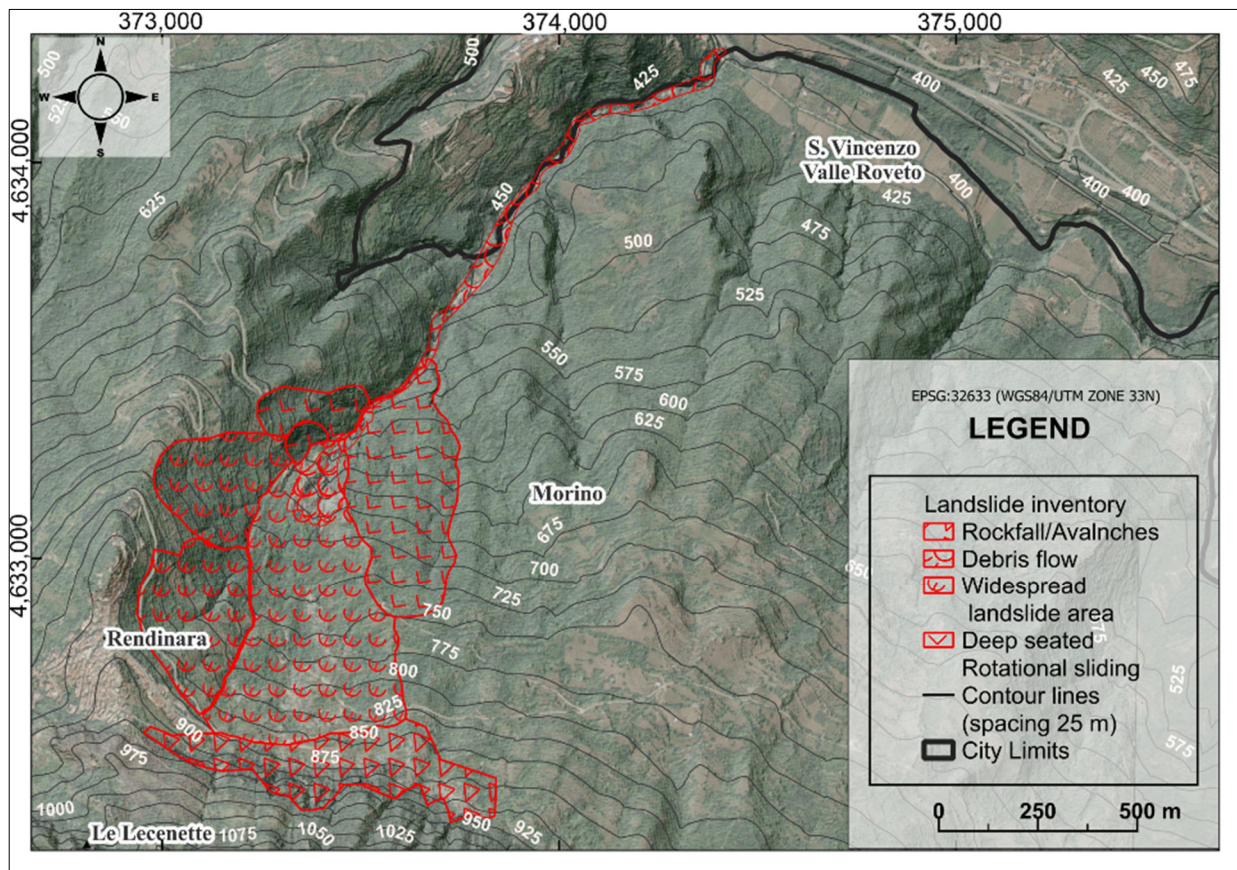
Figure 7. The inventory map was drawn using the results of the study. The image identifies three main mechanisms: a rockfall in the upper part, a deep-seated rotational slide in the central part, and a debris flow in the lower part.

Through MATLAB code [33] analysis of the digital image correlation with Google Earth imagery, two sets of vectors representing the x and y displacement components were obtained. These components were combined to derive the vector representing cumulative displacement, incorporating all relevant geometrical factors, as defined by the following formula:

$$z = Le^{i\theta} \tag{1}$$

$$\sqrt{x_{cumulative}^2 + y_{cumulative}^2} \tag{2}$$

$$\theta = atan2\left(x_{cumulative}^2 + y_{cumulative}^2\right) \tag{3}$$

where z is the polar form of the length vector; L is the length expressed in meters; θ is the angle measured in radians, which indicates the direction of the vector relative to the real (horizontal) axis; $x_{cumulative}$ represents the cumulative component along the x axis; and $y_{cumulative}$ represents the cumulative component along the y axis (R1).

The resulting 2D vectors are illustrated in Figure 8. Analysis of the aliases revealed that the upper sector of the Morino-Rendinara landslide consistently exhibited movement throughout the temporal span covered by the digital image correlation with Google Earth imagery (2016–2022) [16]. Notably, the most significant displacement values were concentrated in the central sector, particularly evident in the debris flow last reactivation source zone. Furthermore, it was observed that the line of displacement closely followed the local topography variation. This observation suggested the presence of a significant slide component influencing this section of the analyzed cascading landslide. Similarly, by observing the displacement direction in the upper sector, it was possible to discern a

rotational component within the landslide. This was evident as the vectors did not follow the maximum slope gradient. Higher rates of displacement were recorded in the median sector of the deep-seated rotational slide. Overall, the displacement ranged from 0 to 10 m, with a mean maximum velocity estimate of 1.66 m/year.
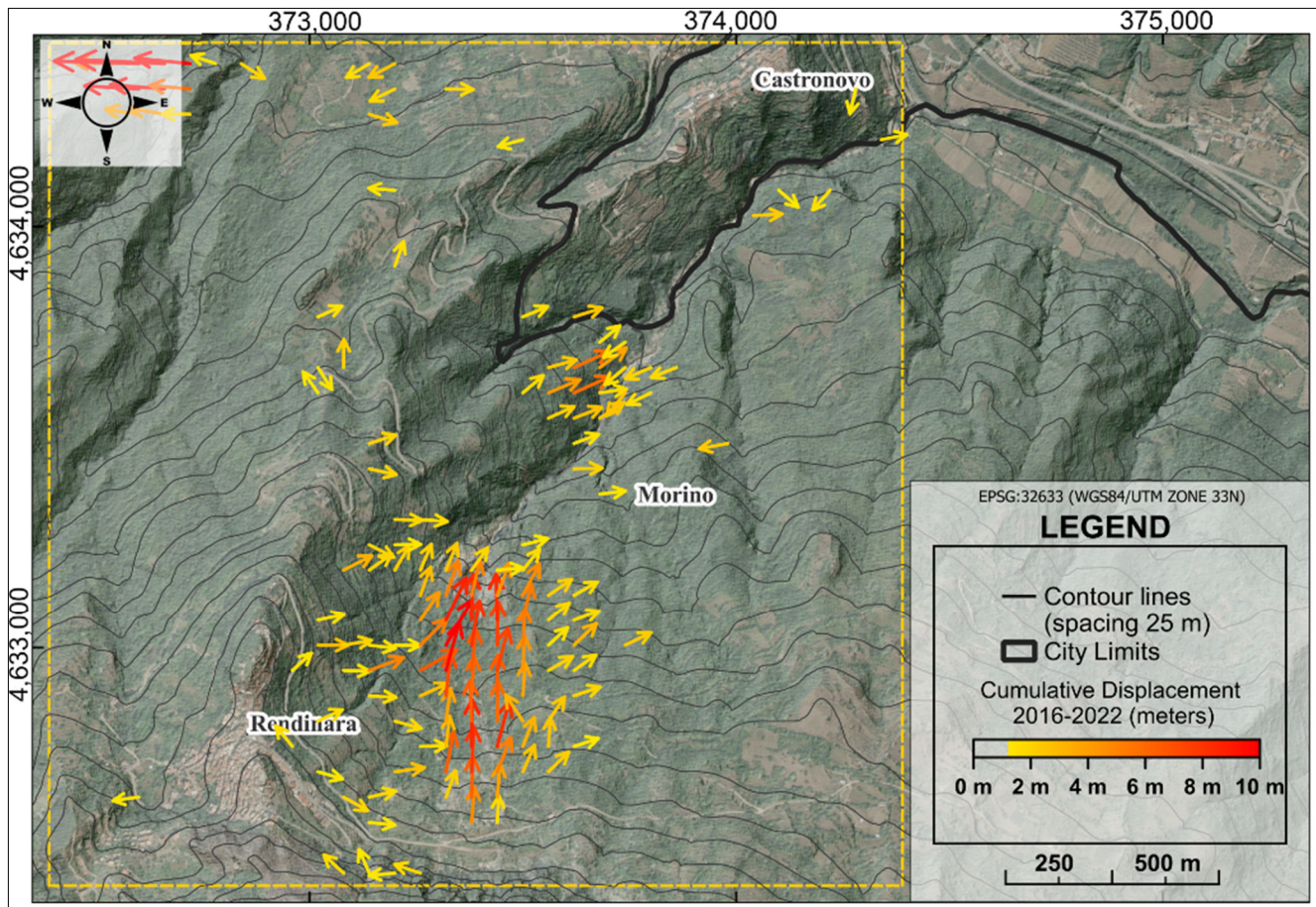

Figure 8. Details of the landslide inventory map. The various fillings show the different landslide types identified in the study area: the rockfall in the upper part, the deep-seated rotational slide in the central part, and the debris flow in the lower part of the slope.

Displacements were equally distributed along the upper part of study area from north to south (Figure 7). This suggested that the main component was reasonably attributed to sliding. Therefore, it was reasonable to consider that there was another component in the kinematics of the landslide, possibly driven by rotational force due to the high displacement values along the left side of the upper sector.

4.2. Interferometric Data Results

Interferometric analysis was also performed. Using the CPT algorithm implemented in Subsidence software, the persistent scatterers (PS) [43] of the area were identified at rock outcrop points, some of which are highlighted in Figure 9.

It is necessary to underline that the latter represent the cumulative displacements starting from the first available image, while the average velocity represents a sort of linear velocity that the model estimates over the entire acquisition interval. It is necessary to observe that, according to the convention commonly adopted, positive values of velocity/displacement are to be interpreted as approaching the satellite (East–West direction for ascending geometry) while negative values are to be interpreted as moving away from the satellite (West–East direction in ascending geometry), always along the LoS [44].
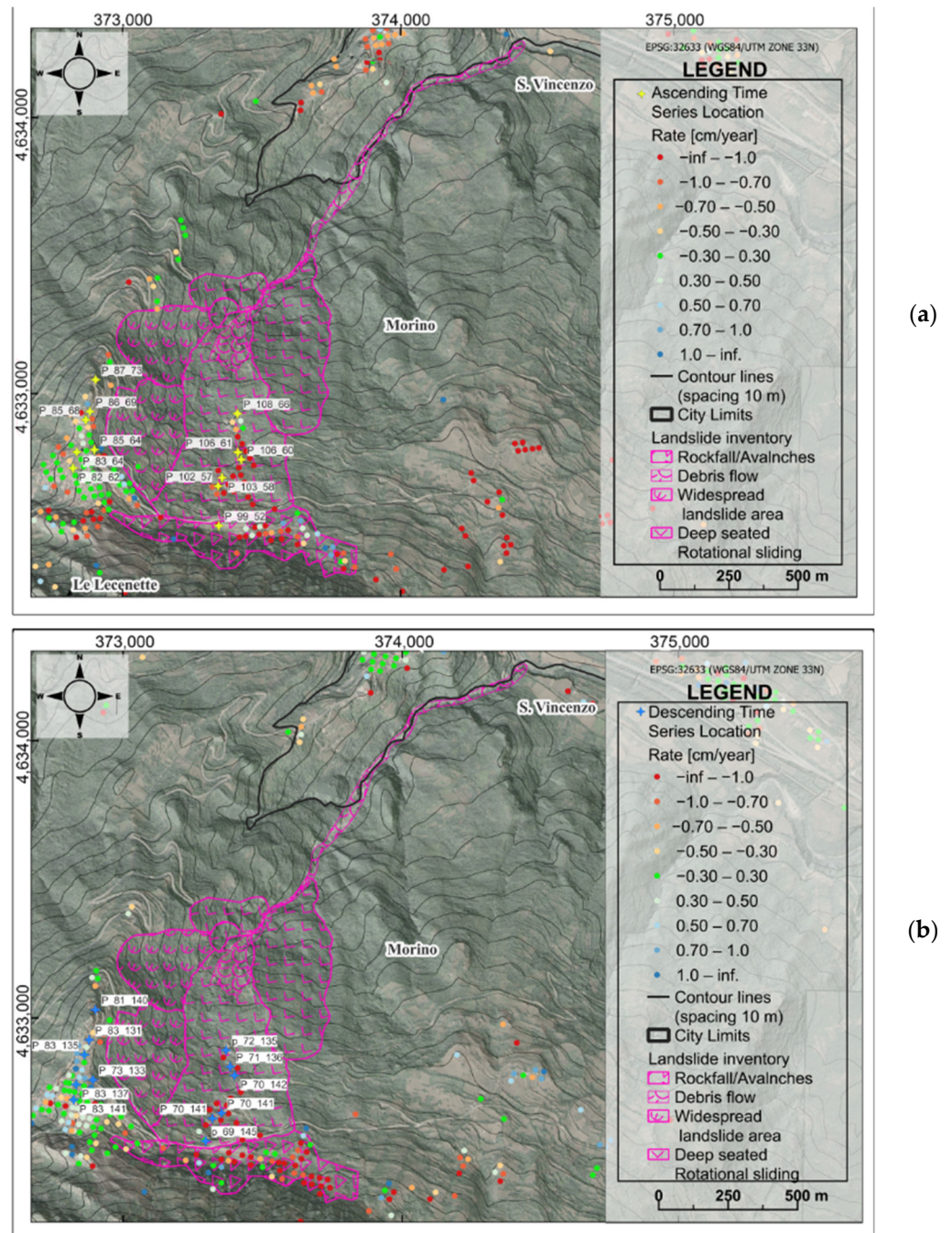
Figure 9. PS velocity along the ascending (**a**) and descending (**b**) geometries from 2020 to 2023. Red dots indicate major velocity trends and instability, green and blue dots indicate minor velocity and stable sectors.

In detail, in the area under consideration, 1257 targets in ascending geometry were identified, which had an average displacement velocity along the LoS of up to about 2.5 cm/year for the period 2020/2023. This value was not homogeneous with respect to the area where, in correspondence with the central sector of the study area affected by the presence of an active landslide, displacements and velocities were greater; thus, these rates fully mirrored the trend of overrunning. Also in this case, it is necessary to observe that, according to the convention commonly adopted, positive values of velocity/displacement are to be interpreted as approaching the satellite (West–East direction in descending geometry) while negative values are to be interpreted as moving away from the satellite (East–West direction in descending geometry), always along the sensor-target line [45]. In detail, in

the area under consideration, numerous targets were identified, which had an average displacement velocity along the LoS of the maximum order of about 1 cm/year, recorded in correspondence with the eastern sector of the study area. Through the cross-correlation between interferometric analyses and field activities, a series of materialized reflectors were selected to reconstruct the time series displacement over the analyzed time span. Given the proximity of Morino Village to the left side of the landslide body, it was crucial to include several reflectors situated in the municipality to identify any potentially critical movements.

Additionally, another set of reflectors was chosen within the landslide body to identify the main displacements. The reflectors in the eastern sector showed an average displacement velocity of the maximum order of a few mm/year (P_85_68, P_83_64, P_82_62 in Figure 9), except for the point showing a marked displacement in ascending geometry, similar to what was found in correspondence with a reflector positioned just west of it identified in descending geometry (P_73_133). A sector where significant displacement rates were evident, and therefore active phenomena, was instead found in the eastern sector of the study area. The identified time series identified a highly active sector represented by significant displacement rates.

The time series analyzed in correspondence with the targets showing higher displacement rates had highlighted values even higher than 2 cm/year, as shown in Figure 10a,b.

4.3. Rainfall Landslide Movement Influence and Slope Stability Analysis

What emerged from the interferometric analyses was connected to what was found from the analyses carried out in the field. In addition to highlighting active kinematics concerning the landslide, it was evident how, in the upper part, there were displacements indicating a possible rotational component or a preferential movement. This aspect is due to variations in underground water circulation associated with increases in thrust due to compression of less permeable layers. Furthermore, there was much evidence attributable to the active tectonics described, with a series of points with high displacement rates aligned along the limestone-clay contact. To underline the important role of water in the state of activity of this landslide, an analyses of rainfall data compared to a representative time series was carried out. Figure 11a shows the monthly cumulative rainfall, Figure 11b shows the daily cumulative rainfall, and Figure 11c shows the cumulative rainfall during all of the interferometric analysis period of 2020–2023.

Peaks, either positive or negative, in the time series indicating landslide movement, corresponded to a high accumulation of rainfall, with a lag time of a few days. This was reasonable given the type of land use and the underground conditions, as there was a very permeable cover layer. The described tendency is well shown in Figure 11b, where associated with December 2020 rainfall, a displacement of approximately 5 cm was recorded. Similarly, the same trend was observed in the descending series associated with December 2021. Additionally, the main reactivations were associated with the periods of highest rainfall, corresponding to September to December and March/April, in line with the local climate trends.
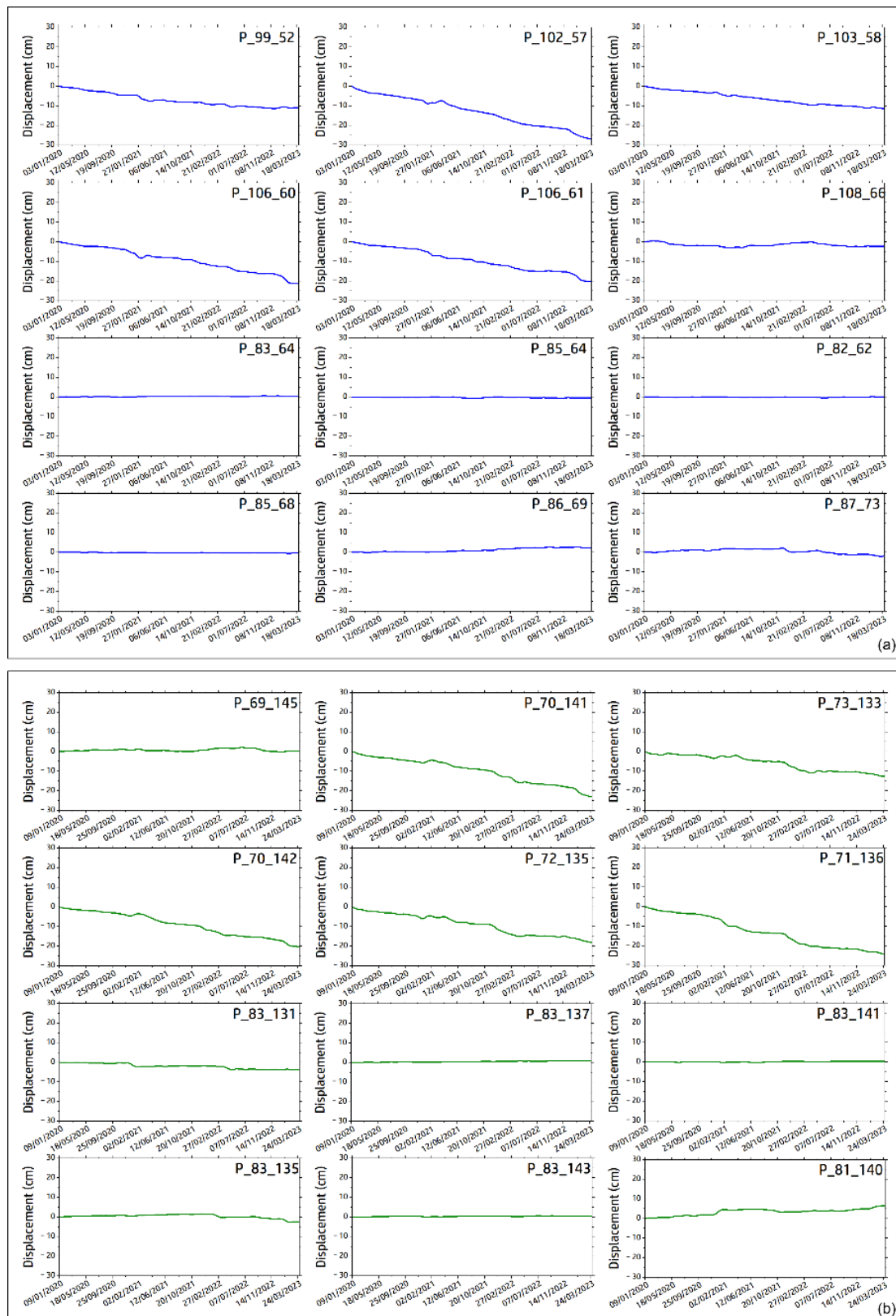
Figure 10. Selected time series in ascending geometry (**a**) and descending geometry (**b**). The analyzed time series illustrates a very unstable sector represented by reflectors P106_60-61 and 102_57 in ascending geometry and P_70_141-141-136 in descending geometry. Additionally, some stable sectors are represented, such as P_83_135-143, P_85_68, and P_86_69.
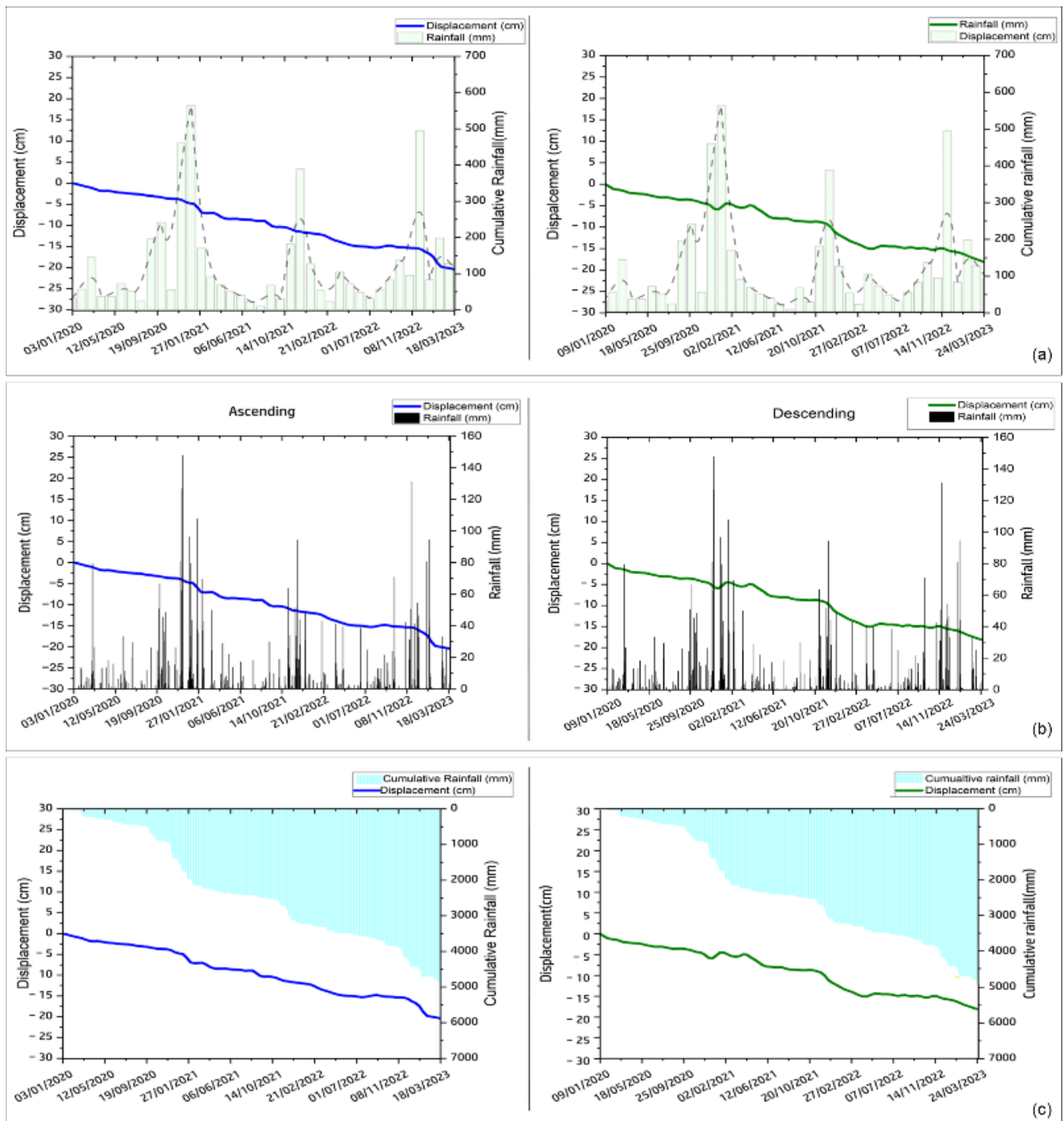
Figure 11. Time series vs. rainfall analyses. (**a**) Monthly cumulative rainfall for analysis period vs. one ascending and descending representative time series; (**b**) Daily cumulative rainfall for analysis period vs. one ascending and descending representative time series; (**c**) Cumulative rainfall for analysis period vs. one ascending and descending representative time series.

According to the combined analysis of time series and rainfall data [40], the results emphasized a significant tendency toward slope instability associated with prolonged periods of intense rainfall. Consequently, several slope stability analyses were carried out, considering water table level fluctuations, which varied with rainfall. An analysis of slope stability was conducted using Adonis software, with four distinct scenarios simulated. These scenarios included water table levels of 6.0, 2.0, and 0.5 m from the surface level,

and one scenario considering no water table influence. The maximum shear strain was estimated to evaluate the degree of shear slipping, primarily represented by the cover layer (Figure 12). The SSI value is commonly employed to identify potential failure surfaces within a slope. It considers the accumulated shear deformation along potential slip surfaces, helping to pinpoint areas most susceptible to mass movements or collapses [46]. In this case, the maximum value was 1.22, and all graphics refer to this value to better underline the difference with water table influence. Figure 12a shows the maximum shear strain values without the water table. In this case, the index was very low, and no specific shear deformation levels were recorded. Figure 12d shows the maximum shear strain values of the model with a water table level of −6.0 m from ground level. Similarly to the first case, no remarkable shear surfaces were recorded, but in the upper-middle sector of the cover layer, a shear deformation zone started to become evident. Figure 12b,c show the highest-influencing water table levels in the model. In both cases, there were two shear strain surfaces for which the area further upstream showed major values of shear strain with a rotational slip surface geometry.
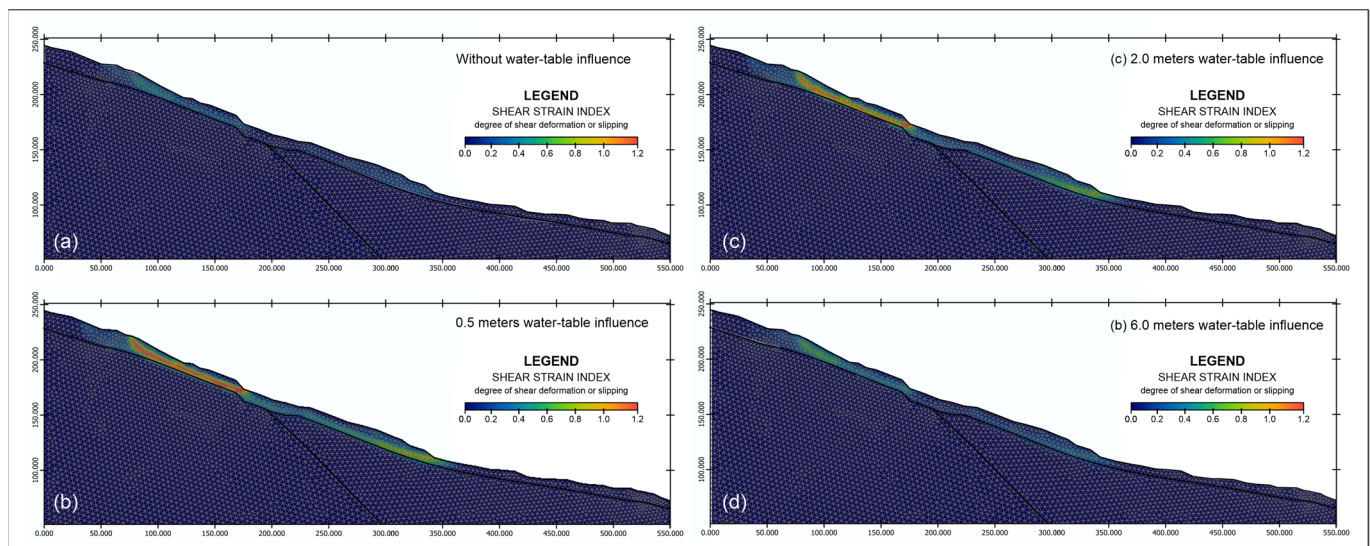

Figure 12. Shear strain index results of the 2D numerical modelling with different pore pressure conditions. (**a**) Analysis without pore pressure; (**b**) Analysis with water table 0.5 m from ground level; (**c**) Analysis with water table 2.0 m from ground level; (**d**) Analysis with water table 6.0 m from ground level.

The results of the FEM model [30] were coherent with the interferometric analysis and pixel offset analysis. Major shear strain levels were recorded where interferometric analysis recorded major displacements and velocities. Similarly, where interferometric analysis did not provide exhaustive information, the pixel offset technique was applied, and the displacements represented along the slope were coherent with the results of the FEM model analysis. In fact, the maximum shear strain rates were concentrated in the upper zone of the slope, where interferometric analysis indicated the presence of unstable persistent scatterers (PS) [24,25], associated with the rotational sliding movements.

5. Discussion

The integration of interferometric techniques, the pixel offset algorithm, and field data provided a detailed and accurate analysis of the Morino-Rendinara landslide dynamics. This approach allowed us to understand the kinematic behavior and highlighted the contributions of both rotational and translational components in different sectors of the area [47]. The interferometric analysis showed the main movements in the upper sector accompanied by significant displacement values in the central sector, where analyses suggested the presence of a rotational component [48]. These results were crossed with

meteorological data, showing a good correlation between displacements and prolonged rainfall periods (Figure 12). The impact of rainfall on landslide activity was demonstrated through the analysis of time series data, correlating rainfall peaks with displacement events [49]. The observed lag time between rainfall events and displacement highlighted the complex interaction between surface hydrology and subsurface conditions.

In this study, the pixel offset technique was used in the areas where interferometric data did not provide exhaustive information. With the pixel offset method, it was possible to analyze the cumulative displacement and the orientation of main displacement vectors. In fact, the results showed a rotational component in the middle sector and a main displacement zone corresponding to the debris flow reactivation source zone. Both the pixel offset and the InSAR techniques have their respective limitations when applied to landslide monitoring. In the case of pixel offset methods, there was reduced applicability in the upper sector of the landslide area. This was primarily due to the presence of rockfalls, which can obscure or distort the imagery, and also because of the orientation of the satellite's image acquisition and positioning. These factors can hinder the accurate detection and measurement of ground displacement in this region. On the other hand, InSAR (Interferometric Synthetic Aperture Radar) also faces intrinsic limitations, particularly related to the orientation of landslides. The technique's effectiveness can be compromised if the displacement is not aligned with the satellite's line of sight, resulting in inaccurate or incomplete data. However, this limitation can be mitigated by installing corner reflectors in the area of interest. These reflectors enhance the radar signal, allowing for more precise measurement of ground movement even in challenging orientations. Furthermore, we analyzed the sections along the line of maximum slope using the FEM approach. The slope stability simulations showed the potential failure surfaces and the influence of water table fluctuations on landslide dynamics [50]. In this case, the FEM analysis complemented interpretations based on interferometric and pixel offset data, highlighting the geometry of sliding and the location of main forces along the slope. These results were consistent with the preliminary geological hypothesis and the literature of a similar study case [14,23] in which water circulation considerably influenced the global stability of the slope. In fact, the area is characterized by a highly fractured carbonaceous aquifer in contact with a less permeable marly aquifer and an unstable heterogeneous cover layer. In a subsequent phase, this study will evolve into the development of a customized monitoring system tailored to the specific needs of the Morino-Rendinara cascading landslide. This system will integrate the findings from the current investigation with advanced analytical approaches to provide continuous and real-time monitoring of landslide activity. By incorporating state-of-the-art sensor technologies, data analysis techniques, and predictive modeling, the system aims to enhance the accuracy and reliability of landslide prediction. The integration of these analytical methods with the comprehensive understanding gained from the current study will enable the identification of early warning signals and contribute to more effective mitigation strategies. This evolution toward a more sophisticated monitoring framework will bridge the gaps identified in the current research, particularly in understanding rockfall dynamics, and will provide a robust platform for ongoing risk assessment and landslide management in the area.

6. Conclusions

This work provides insight into the kinematics and mechanisms of the Morino-Rendinara cascading landslide, employing a comprehensive approach integrating drone surveys, field activities, satellite data, and numerical modeling. The study improves the comprehension of the distinct kinematic patterns and underlying mechanisms contributing to landslide activity in the area. The use of Google Earth high-resolution digital images enabled the precise identification and mapping of unstable areas, active sliding zones, and deformative structures. However, it is important to note that the investigation into rockfall dynamics was limited due to the limitations of the methodologies employed, which are less suited for assessing such phenomena. Integration of traditional field activities with

remote sensing techniques facilitated a comprehensive understanding of the temporal evolution of the landslide events. Analysis of displacement patterns and FEM stability revealed a strong correlation with rainfall events, underscoring the influence of precipitation on landslide dynamics. Peaks in displacement corresponded to periods of high rainfall accumulation, with a lag time of a few days, highlighting the role of water in triggering landslide movements and water's effect on the shear deformation index. The study also identified significant displacement rates and active kinematics in specific sectors, including evidence of rotational slide and debris flow. However, further research is needed to explore the dynamics of rockfall more comprehensively, potentially through alternative methodologies better suited to assessing such phenomena. This work emphasizes the importance of employing advanced technologies and comprehensive methodologies in landslide monitoring and risk assessment. Future research focusing on long-term monitoring and predictive modeling could play a crucial role in enhancing our understanding of landslide behavior. Such research is essential for the design and implementation of a specifically tailored monitoring system for the Morino-Rendinara cascading landslide. By building on the insight gained from this study, a dedicated monitoring system can be developed to accurately assess the landslide's dynamics in real time. This system would incorporate advanced sensor technologies, data analysis methods, and predictive tools, enabling precise dimensioning and deployment. Ultimately, this approach would lead to more effective mitigation strategies and better risk management in landslide-prone areas.

References

1. Hungr, O.; Leroueil, S.; Picarelli, L. The Varnes Classification of Landslide Types, an Update. *Landslides* **2014**, *11*, 167–194. [CrossRef]
2. Kirschbaum, D.B.; Adler, R.; Hong, Y.; Hill, S.; Lerner-Lam, A. A Global Landslide Catalog for Hazard Applications: Method, Results, and Limitations. *Nat. Hazards* **2010**, *52*, 561–575. [CrossRef]
3. Smith, K.; Petley, D.N. *Environmental Hazards: Assessing Risk and Reducing Disaster*; Routledge: London, UK, 2013.
4. Wu, Z.; Barosh, P.J.; Ha, G.; Yao, X.; Xu, Y.; Liu, J. Damage Induced by the 25 April 2015 Nepal Earthquake in the Tibetan Border Region of China and Increased Post-Seismic Hazards. *Nat. Hazards Earth Syst. Sci.* **2019**, *19*, 873–888. [CrossRef]
5. Abbate, A.; Longoni, L.; Ivanov, V.I.; Papini, M. Wildfire Impacts on Slope Stability Triggering in Mountain Areas. *Geosciences* **2019**, *9*, 417. [CrossRef]
6. Varnes, D. Slope Movement Types and Processes. *Spec. Rep.* **1978**, *176*, 11–33.
7. Iverson, R.M.; Reid, M.E.; LaHusen, R.G. Debris-Flow Mobilization from Landslides. *Annu. Rev. Earth Planet. Sci.* **1997**, *25*, 85–138. [CrossRef]
8. Fell, R.; Glastonbury, J.; Hunter, G. Rapid Landslides: The Importance of Understanding Mechanisms and Rupture Surface Mechanics. *Q. J. Eng. Geol. Hydrogeol.* **2007**, *40*, 9–27. [CrossRef]
9. Iverson, R.M.; George, D.L.; Allstadt, K.; Reid, M.E.; Collins, B.D.; Vallance, J.W.; Schilling, S.P.; Godt, J.W.; Cannon, C.M.; Magirl, C.S.; et al. Landslide Mobility and Hazards: Implications of the 2014 Oso Disaster. *Earth Planet. Sci. Lett.* **2015**, *412*, 197–208. [CrossRef]
10. Turner, A.K. Social and Environmental Impacts of Landslides. *Innov. Infrastruct. Solut.* **2018**, *3*, 70. [CrossRef]

11. Pudasaini, S.P.; Krautblatter, M. The Landslide Velocity. *Earth Surf. Dyn.* **2022**, *10*, 165–189. [CrossRef]

12. Allen, S.K.; Rastner, P.; Arora, M.; Huggel, C.; Stoffel, M. Lake Outburst and Debris Flow Disaster at Kedarnath, June 2013: Hydrometeorological Triggering and Topographic Predisposition. *Landslides* **2016**, *13*, 1479–1491. [CrossRef]

13. Usamah, M. *Analysis of the Causal and Trigger Factors of the August 2017 Landslide in Freetown: Towards a Sustainable Landslide Risk Management in Sierra Leone*; United Nations Development Program (UNDP) and Environmental Protection Agency (EPA): New York, NY, USA, 2017.

14. Zito, C.; Mangifesta, M.; Francioni, M.; Guerriero, L.; Di Martire, D.; Calcaterra, D.; Pasculli, A.; Sciarra, N. Cascading landslide at Morino-Rendinara, L'Aquila, Central Italy: Numerical modelling of slope-scale prospective debris flow propagation. *Ital. J. Eng. Geol. Environ.* **2024**, 285–293. [CrossRef]

15. Bouzid, D.A. Finite Element Analysis of Slope Stability by Expanding the Mobilized Principal Stress Mohr's Circles—Development, Encoding and Validation. *J. Rock Mech. Geotech. Eng.* **2022**, *14*, 1165–1179. [CrossRef]

16. Google Earth Pro 7.3.6.9796. (February 22, 2024). Morino-Rendinara, Italy. 41°50′25.50″N, 13°28′28.79″E. Digital Globe August 2021 and March 2022. Available online: www.google.com/earth/index.html (accessed on 1 March 2024).

17. Saroli, M.; Biasini, A.; Cavinato, G.P.; Di Luzio, E. Geological Setting of the Southern Sector of the Roveto Valley (Central Apennines, Italy). *Boll. Della Soc. Geol. Ital.* **2003**, *122*, 467–481.

18. Fabbi, S. Geology of the Eastern Slopes of the Simbruini Mts. Between Verrecchie and Capistrello (Central Apennines—Abruzzo, Italy). *J. Maps* **2018**, *14*, 435–446. [CrossRef]

19. Parotto, M. Stratigrafy and Tectonics of the Eastern Simbruini and Western Marsica Ranges (Central Apennines—Italy). *Atti Accad. Naz. Lincei* **1971**, *8*, 93–170.

20. Maceroni, D.; Dixit Dominus, G.; Gori, S.; Falcucci, E.; Galadini, F.; Moro, M.; Saroli, M. First Evidence of the Late Pleistocene—Holocene Activity of the Roveto Valley Fault (Central Apennines, Italy). *Front. Earth Sci.* **2022**, *10*, 1018737. [CrossRef]

21. Cosentino, D.; Cipollari, P. The Messinian Central Apennines. *Rend. Online Soc. Geol. Ital.* **2012**, *23*, 45–51.

22. CARG Project in Geological Itanlian Chart 1:100,000 Foglio Carta Geologica d'Italia 1:100,000 n. 152 Sora Progetto—CARG. 1976. Available online: https://sgi.isprambiente.it/geologia100k/mostra_foglio.aspx?numero_foglio=152 (accessed on 1 March 2024).

23. Sciarra, N.; Mangifesta, M.; Carabba, L.; Mischiatti, L. Methodological Approach for the Study of Historical Centres of High Architectural Value Affected by Geo-Hydrological Hazards: The Case of Lanciano (Abruzzo Region—Central Italy). *Geosciences* **2022**, *12*, 193. [CrossRef]

24. Costantini, M.; Ferretti, A.; Minati, F.; Falco, S.; Trillo, F.; Colombo, D.; Novali, F.; Malvarosa, F.; Mammone, C.; Vecchioli, F.; et al. Analysis of Surface Deformations over the Whole Italian Territory by Interferometric Processing of ERS, Envisat and COSMO-SkyMed Radar Data. *Remote Sens. Environ.* **2017**, *202*, 250–275. [CrossRef]

25. Mora, P.; Baldi, P.; Casula, G.; Fabris, M.; Ghirotti, M.; Mazzini, E.; Pesci, A. Global Positioning Systems and Digital Photogrammetry for the Monitoring of Mass Movements: Application to the Ca' Di Malta Landslide (Northern Apennines, Italy). *Eng. Geol.* **2003**, *68*, 103–121. [CrossRef]

26. Mallorqui, J.J.; Mora, O.; Blanco, P.; Broquetas, A. Linear and Non-Linear Long-Term Terrain Deformation with DInSAR (CPT: Coherent Pixels Technique). In Proceedings of the FRINGE 2003 Workshop (ESA SP-550), Frascati, Italy, 1–5 December 2003.

27. Guerriero, L.; Di Martire, D.; Calcaterra, D.; Francioni, M. Digital Image Correlation of Google Earth Images for Earth's Surface Displacement Estimation. *Remote Sens.* **2020**, *12*, 3518. [CrossRef]

28. Zheng, H.; Tian, B.; Liu, D.F.; Feng, Q. Definitions of Safety Factor of Slope Stability Analysis with Finite Element Method. *Yanshilixue Yu Gongcheng Xuebao Chin. J. Rock Mech. Eng.* **2005**, *24*, 2225–2230.

29. Geraili Mikola, R. ADONIS: A Free Finite Element Analysis Software with an Interactive Graphical User Interface for Geoengineers. In Proceedings of the GeoOttawa 2017, Ottawa, ON, Canada, 1–4 October 2017.

30. Chen, B. Finite Element Strength Reduction Analysis on Slope Stability Based on ANSYS. *Environ. Earth Sci. Res. J.* **2017**, *4*, 60–65. [CrossRef]

31. Quamar, M.M.; Al-Ramadan, B.; Khan, K.; Shafiullah, M.; El Ferik, S. Advancements and Applications of Drone-Integrated Geographic Information System Technology—A Review. *Remote Sens.* **2023**, *15*, 5039. [CrossRef]

32. Iglesias, R.; Mallorqui, J.J.; Monells, D.; López-Martínez, C.; Fabregas, X.; Aguasca, A.; Gili, J.A.; Corominas, J. PSI Deformation Map Retrieval by Means of Temporal Sublook Coherence on Reduced Sets of SAR Images. *Remote Sens.* **2015**, *7*, 530–563. [CrossRef]

33. The MathWorks Inc. MATLAB. 2023. Available online: https://it.mathworks.com/products/matlab.html (accessed on 1 March 2024).

34. Cascini, L.; Fornaro, G.; Peduto, D. Advanced Low- and Full-Resolution DInSAR Map Generation for Slow-Moving Landslide Analysis at Different Scales. *Eng. Geol.* **2010**, *112*, 29–42. [CrossRef]

35. Sato, H.P.; Harp, E.L. Interpretation of Earthquake-Induced Landslides Triggered by the 12 May 2008, M7.9 Wenchuan Earthquake in the Beichuan Area, Sichuan Province, China Using Satellite Imagery and Google Earth. *Landslides* **2009**, *6*, 153–159. [CrossRef]

36. QuantumGis 3.18 Geographic Information System; QGIS Association 2023. Available online: www.qgis.org (accessed on 1 March 2024).

37. Berger, M. *Geometry I*; Springer: Berlin/Heidelberg, Germany, 1987; ISBN 3-540-11658-3.

38. Govender, N. *Evaluation of Feature Detection Algorithms for Structure from Motion*; CSIR: Pretoria, South Africa, 2009.

39. Lucas, B.; Kanade, T. An iterative image registration technique with an application to stereo vision. In Proceedings of the 7th International Joint Conference on Artificial Intelligence, San Francisco, CA, USA, 24–28 August 1981; pp. 674–679.

40. Regione Abruzzo—Servizio Idrografico e Mareografico. Available online: https://www.regione.abruzzo.it/content/servizio-idrografico-mareografico (accessed on 1 March 2024).

41. Mohammadi, S. *Extended Finite Element Method: For Fracture Analysis of Structures*; John Wiley & Sons: Hoboken, NJ, USA, 2008.

42. Guerriero, L.; Guadagno, F.M.; Revellino, P. Estimation of Earth-Slide Displacement from GPS-Based Surface-Structure Geometry Reconstruction: Estimation of Earth-Slide Displacement. *Landslides* **2019**, *16*, 425–430. [CrossRef]

43. Gabriel, A.K.; Goldstein, R.M.; Zebker, H.A. Mapping Small Elevation Changes over Large Areas: Differential Radar Interferometry. *J. Geophys. Res.* **1989**, *94*, 9183–9191. [CrossRef]

44. Casagli, N.; Catani, F.; Del Ventisette, C.; Luzi, G. Monitoring, Prediction, and Early Warning Using Ground-Based Radar Interferometry. *Landslides* **2010**, *7*, 291–301. [CrossRef]

45. Di Martire, D.; Novellino, A.; Tessitore, S.; Ramondini, M.; Calcaterra, D. Application of DInSAR Techniques to Engineering Geology Studies in Southern Italy. *Rend. Online Soc. Geol. Ital.* **2013**, *24*, 95–97.

46. Morgenstern, N.R.; Price, V.E.; Morgenstern, N.R.; Price, V.E. The Analysis of the Stability of General Slip Surfaces. *Géotechnique* **1965**, *15*, 79–93. [CrossRef]

47. Bianchini, S.; Solari, L.; Bertolo, D.; Thuegaz, P.; Catani, F. Integration of Satellite Interferometric Data in Civil Protection Strategies for Landslide Studies at a Regional Scale. *Remote Sens.* **2021**, *13*, 1881. [CrossRef]

48. Khandelwal, D.D.; Gahalaut, V.; Kumar, N.; Kundu, B.; Yadav, R.K. Seasonal Variation in the Deformation Rate in NW Himalayan Region. *Nat. Hazards* **2014**, *74*, 1853–1861. [CrossRef]

49. Guo, Z.; Ferrer, J.V.; Hürlimann, M.; Medina, V.; Puig-Polo, C.; Yin, K.; Huang, D. Shallow Landslide Susceptibility Assessment under Future Climate and Land Cover Changes: A Case Study from Southwest China. *Geosci. Front.* **2023**, *14*, 101542. [CrossRef]

50. Van den Bout, B.; Lombardo, L.; Chiyang, M.; van Westen, C.; Jetten, V. Physically-Based Catchment-Scale Prediction of Slope Failure Volume and Geometry. *Eng. Geol.* **2021**, *284*, 105942. [CrossRef]